



# One-pot synthesis of CdS@Nb<sub>2</sub>O<sub>5</sub> core-shell nanostructures with enhanced photocatalytic activity

Luiz C.A. Oliveira<sup>a,\*</sup>, Henrique S. Oliveira<sup>a</sup>, Giovanna Mayrink<sup>a</sup>, Herman S. Mansur<sup>b</sup>, Alexandra A.P. Mansur<sup>b</sup>, Roberto Luiz Moreira<sup>c</sup>

<sup>a</sup> Department of Chemistry, ICEx, Federal University of Minas Gerais, Av. Antonio Carlos, 6627, Pampulha, Belo Horizonte CEP 31270-901, MG, Brazil

<sup>b</sup> Center of Nanoscience, Nanotechnology and Innovation-CeNano I, Department of Metallurgical and Materials Engineering, School of Engineering, Federal University of Minas Gerais, Av. Antonio Carlos, 6627, Pampulha, Belo Horizonte CEP 31270-901, MG, Brazil

<sup>c</sup> Department of Physics, ICEx, Federal University of Minas Gerais, Av. Antonio Carlos, 6627, Pampulha, Belo Horizonte CEP 31270-901, MG, Brazil

## ARTICLE INFO

### Article history:

Received 28 September 2013

Received in revised form 7 January 2014

Accepted 14 January 2014

Available online 5 February 2014

### Keywords:

Nanostructured materials

Semiconductor nanoparticles

Photo-oxidation

Environmental process

## ABSTRACT

CdS@Nb<sub>x</sub>O<sub>y</sub> core-shell nanostructures were used as heterogeneous catalysts for oxidizing organic compounds in aqueous media under ultraviolet light. The core/shell nanocrystals contained two nanostructured semiconductor that enhanced the catalytic properties of the material under UV–Vis irradiation. The developed core/shell nanocrystals displayed significant catalytic activity during the oxidation of organic substrates and may be suitable for degrading organic pollutants in water. The ESI–MS spectrum obtained for methylene blue after exposure to the nanostructured semiconductor nanoparticles revealed a hydroxylation caused by hydroxyl radicals in solution, forming a species at  $m/z = 301$ .

© 2014 Elsevier B.V. All rights reserved.

## 1. Introduction

New materials with high pollutant removal capacities and recyclability have contributed significantly to the treatment of contaminated effluents [1–3]. Catalytic systems based on Nb<sub>2</sub>O<sub>5</sub> and CdS received special attention mainly due to their promising catalytic activity in several important chemical processes, particularly in processes requiring high acidity [4–8]. In spite of the interest in applying niobium compounds, their chemical properties are not completely known, much like those of other metals commonly used in industry [1].

The growing concern about water resources has directed the interest of researchers toward the development of new industrial effluent treatment technologies that are more efficient and less onerous; this research has intensified the studies using niobium compounds because Brazil is among the largest producers of this material. Additionally, the textile industry generates excessive quantities of effluents that might cause serious environmental contamination [2–8]. Textile dyes must exhibit high chemical stability because they must be applied permanently to a medium without color alteration. Therefore, these compounds are not easily

removed through traditional effluent treatment processes, causing serious damage to the aquatic system [9,10].

“Advanced Oxidation Processes” (AOP) are promising water and effluent treatment technologies capable of decreasing or eliminating the toxicity of organic compounds. These processes utilize *in situ*-generated hydroxyl radicals that are highly reactive toward organic molecules. Photocatalysis employing semiconductors, such as TiO<sub>2</sub>, in the presence of ultraviolet radiation is a highly studied AOP [11,12].

Niobium-based catalysts have proven efficiency during the total oxidation of organic compounds in aqueous media in the presence of ultraviolet or even sunlight [13]. Using solar radiation is highly desirable because it makes the process more economically viable. However, the classic photocatalyst, TiO<sub>2</sub>, exhibits a low radical generation capacity under solar irradiation. Therefore, MgO, WO<sub>3</sub>, ZnO, niobium oxides (Nb<sub>2</sub>O<sub>5</sub>, NbO<sub>2</sub>, NbO) and their derivative catalysts have been employed with relative success in different reaction systems [13–16]. Moreover, metal oxides may be combined with other materials, such as semiconductors, to improve their overall performance. Metal chalcogenide (MC) nanocrystals (NCs) type II–VI ( $M = \text{Cd}^{2+}$ ,  $\text{Pb}^{2+}$ ,  $\text{Zn}^{2+}$ ,  $X = \text{S}^{2-}$ ,  $\text{Se}^{2-}$ ,  $\text{Te}^{2-}$ ) have been frequently chosen as semiconductors due to their unique optical properties in the visible range of the electromagnetic spectrum, and their potential for multiple applications in catalysts and light emitting devices.

\* Corresponding author. Tel.: +55 31 34097550; fax: +55 31 34095700.

E-mail address: [luizoliveira@qui.ufmg.br](mailto:luizoliveira@qui.ufmg.br) (L.C.A. Oliveira).

In this work, we report a new system based on CdS@Nb<sub>2</sub>O<sub>5</sub> core-shell nanostructures with good catalytic activity for photocatalysis under visible radiation. The aims of this work were to synthesize and evaluate niobium-modified cadmium sulfide in the oxidation of a model molecule (methylene blue dye) in the presence of visible radiation and the identification of reaction intermediates by electrospray ionization mass spectrometry (ESI-MS).

## 2. Experimental

### 2.1. Catalysts preparation

The CdS and CdS-Nb<sub>x</sub>O<sub>y</sub> nanostructures were synthesized using an aqueous route in a reaction flask using stock solutions of cadmium (Cd(ClO<sub>4</sub>)<sub>2</sub>·6H<sub>2</sub>O, 1 × 10<sup>-2</sup> mol L<sup>-1</sup>), sulfur (CH<sub>3</sub>CSNH<sub>2</sub>, 8 × 10<sup>-3</sup> mol L<sup>-1</sup>), and niobium precursors (NH<sub>4</sub>(NbO(C<sub>2</sub>O<sub>4</sub>)<sub>2</sub>(H<sub>2</sub>O)<sub>2</sub>)(H<sub>2</sub>O)<sub>3</sub>), 1 × 10<sup>-2</sup> mol L<sup>-1</sup>) and NaOH solution (1.0 mol L<sup>-1</sup>) for adjusting the pH.

The CdS nanocrystals (referred to as S4) were synthesized using an aqueous, homogenous precipitation route. The Cd<sup>2+</sup> and S<sup>2-</sup> precursors were mixed in a 1:1 ratio as follows: under moderate magnetic stirring, 100 mL thioacetamide solution was added dropwise into 80 mL cadmium precursor solution. Subsequently, the pH was adjusted to 13.0 ± 0.1 by addition of 1.0 mol L<sup>-1</sup> sodium hydroxide solution dropwise (~15–17 mL) and CdS precipitated almost instantaneously. To synthesize the CdS-Nb<sub>x</sub>O<sub>y</sub> nanostructures (referred to as S5 and S6, depending on the amount of Nb<sup>5+</sup> related to Cd<sup>2+</sup>, 5% and 10%, respectively), 4 mL (S5) or 8 mL (S6) niobium precursor (oxalate salt) solution was gently added to the reaction flask containing 80 mL of Cd<sup>2+</sup> and 100 mL of S<sup>2-</sup> solutions, as previously prepared for S4, before raising the pH to 13.0 ± 0.1 (NaOH solution, 1.0 mol L<sup>-1</sup>). As the pH of the medium rose, the CdS nanocrystal precipitates acted as “seeds,” nucleating the hydrated niobium oxide (Nb<sub>2</sub>O<sub>5</sub>·*n*H<sub>2</sub>O) and forming core-shell structures (CdS@Nb<sub>2</sub>O<sub>5</sub>·*n*H<sub>2</sub>O) (Fig. 1). These precipitates were filtered, washed with copious DI water and dried in an oven at (110 ± 5) °C for 48 h before characterization and use in photocatalytic assays.

### 2.2. Catalysts characterization

Fourier Transform Infrared (FTIR) spectroscopy was performed on a Thermo-Nicolet Nexus 470 spectrometer either by conventional transmission through pressed pellets 13 mm in diameter containing 1.5 mg of dry, powdered samples in KBr (300 mg) matrices or by attenuated total reflection (micro-ATR, with a 300 μm ZnSe crystal) on a Cassegrain microscope (Centaurus, 10× magnification) in reflection mode. The spectra were collected in the middle infrared range (550–4000 cm<sup>-1</sup>), under nitrogen by averaging 64 scans. The spectral resolution was better than 4 cm<sup>-1</sup>.

Raman scattering spectra were collected on a Dilor-XY triple-monochromator equipped with a LN<sub>2</sub>-cooled CCD detector and an Olympus microscope (100× objective). The spectral resolution was ca. 1 cm<sup>-1</sup>, and the lateral resolution (spot size) was 1 μm. The measurements were carried out in the back-scattering geometry while using the 647 nm line of a He–Cd laser (3 mW on the sample's surface) as the excitation source. The spectra were obtained between 80 and 1200 cm<sup>-1</sup> by averaging three 60 s accumulations (80–450 cm<sup>-1</sup>) or five 120 s accumulations (450–700 and 750–1200 cm<sup>-1</sup>).

XRD assays were conducted with an X'Pert instrument (PANalytical) that used KαCu radiation at λ = 1.5406 Å in a 2θ range of 3° to 90° with a 0.02° step.

The N<sub>2</sub> adsorption/desorption isotherms were obtained at 77 K in an Autosorb 1 Quantachrome apparatus. The sample was first

treated at 300 °C under flowing nitrogen for 3 h. The pore size distribution was calculated from the isotherm using the BJH method. The specific surface area was calculated using the BET equation in the area of low relative pressure (*p/p*<sup>o</sup> = 0.200).

The diffuse reflectance spectrum was taken using dry, ground powders using a Varian Cary 5 spectrophotometer equipped with a diffuse reflectance apparatus.

The emission spectra of the CdS and CdS-Nb<sub>2</sub>O<sub>5</sub> nanocrystals were acquired with a Nanodrop 3300 fluoro-spectrometer (Thermo Scientific). The excitation source was a solid-state white light emitting diode with λ<sub>excitation</sub> = 460–650 nm. All photoluminescence (PL) spectra were collected at room temperature. The fluorescence measurements were reported in relative fluorescent units (RFU) based on the fluorescence at the wavelength where the emission spectra had reached their maximum intensity. The relative activity was calculated by subtracting the backgrounds of the samples without (Quantum dots) QDs. The tests were performed using at least four replicates (*n* ≥ 4). Additionally, the QD colloidal media were placed inside a “darkroom-chamber” where they were illuminated with an UV radiation emission bulb (λ<sub>excitation</sub> = 245 nm, 6 W, Boitton Instruments). Digital color images were collected when the QDs fluoresced in the visible range.

### 2.3. Catalytic tests

Methylene blue (MB) is a cationic dye used as a model compound in oxidation reactions that exhibits a strong absorption in the visible region (λ<sub>max</sub> = 665 nm), high solubility in water and properties similar to those of the textile dyes that are difficult to degrade.

The catalytic tests were carried out at 25 °C with 80.0 mL of a solution containing 50 mg L<sup>-1</sup> of MB dye and 60.0 mg of the material (catalyst). A high-pressure mercury lamp (HPK 125 W-Philips) with a water-cooled filter was the UV light source. A 300 W xenon lamp with a cutoff filter was used as the visible light irradiation source.

The oxidation efficiency was monitored with UV-Vis spectroscopy (Shimadzu-UV-1601 PC) at 665 nm to observe a characteristic peak for the MB dye.

To identify the intermediate chemical species formed during the methylene blue oxidation reaction, an ION-TRAP LCQ Fleet (ThermoScientific, San Jose, CA) was used in positive ion mode. The reaction samples were analyzed by introducing aliquots into the ESI-MS source using a syringe pump at 15 L min<sup>-1</sup>. Total Organic Carbon (TOC) measurements were carried out in TOC 500A Shimadzu.

## 3. Results and discussion

### 3.1. Catalysts characterization

The materials were characterized using different techniques to form a better understanding of the catalytic processes involved. The Raman spectra obtained for the investigated samples are presented in Fig. 2 with their characteristic peak positions as indicated. In the CdS sample (S4), four peaks were clearly observed: 148, 213, 301, and 595 cm<sup>-1</sup>. These peaks could be attributed to crystalline CdS with a wurtzite structure, as follows: the 301 cm<sup>-1</sup> band is a convolution of two close polar modes with independent symmetries (A1-LO and E1-LO) that cannot be resolved in powder samples [17], the 595 cm<sup>-1</sup> mode is a combined mode that is most likely an A1 type 2ν<sub>LO</sub> (double phonon of the 301 cm<sup>-1</sup> mode) [18], the 213 cm<sup>-1</sup> band must be a defect-activated mode of the B2 symmetry (this mode also appears in bulky crystals associated to polar defects) [19], and, finally, the 148 cm<sup>-1</sup> band appears to be a zone edge phonon [20]. While the three higher frequency bands appeared in the spectra of S5 and S6 samples as well, the lowest

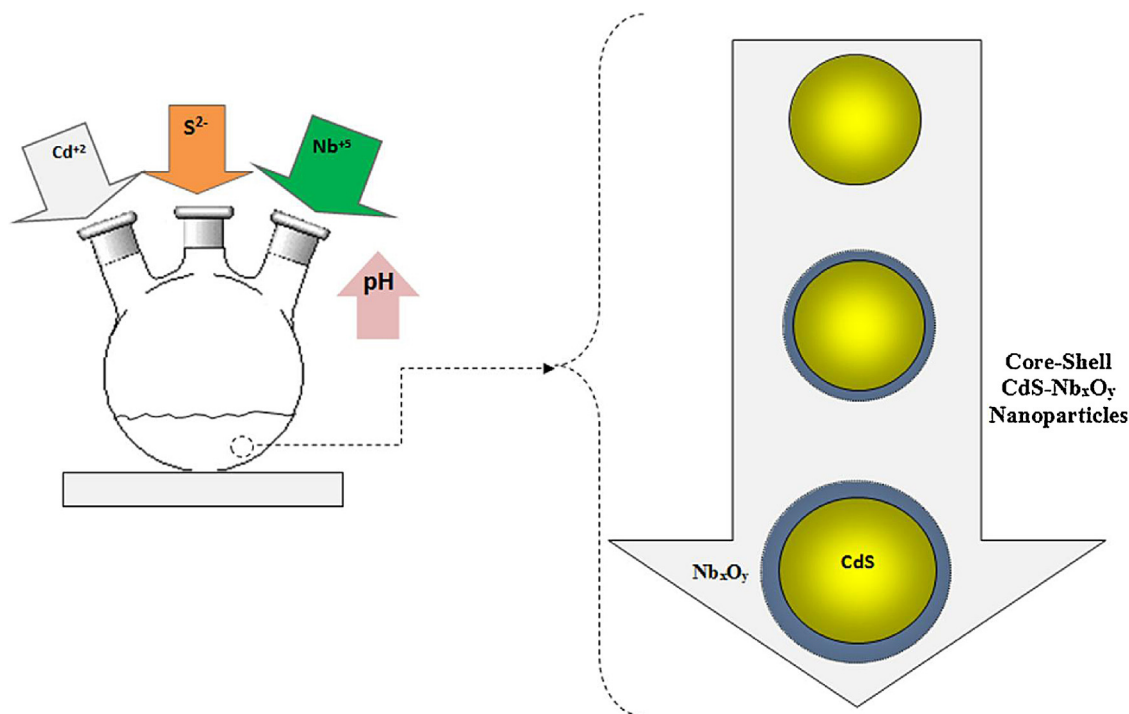


Fig. 1. Steps of the synthesis of the core-shell nanostructured material.

frequency mode decreased in relative intensity between S4 and S5 before disappearing in S6, which has the highest niobium content. This result suggests that the different behaviors of the  $148\text{ cm}^{-1}$  mode might indicate a decreasing NC size from S4 to S6. A zone edge phonon was observed at low temperatures ( $100\text{ K}$ ) in CdS crystals at  $151\text{ cm}^{-1}$  and attributed to a LA mode at the Brillouin M-point [20], making it consistent with the high calculated density of states for this mode [21]. A decreasing crystallite size would influence the conservation of momentum for the off-center phonons, similar to this case (once momentum conservation is assured by a reciprocal lattice vector).

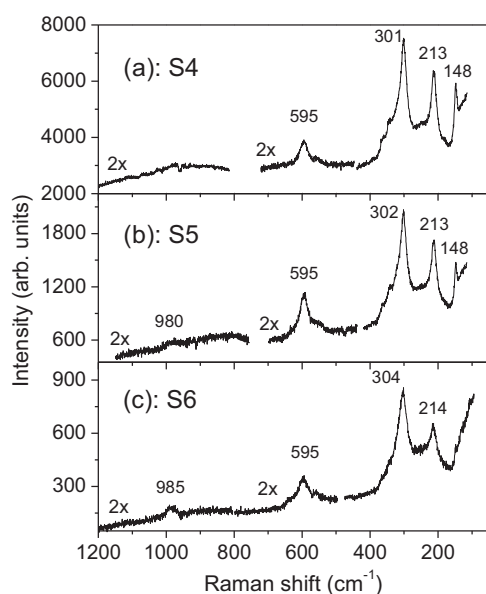
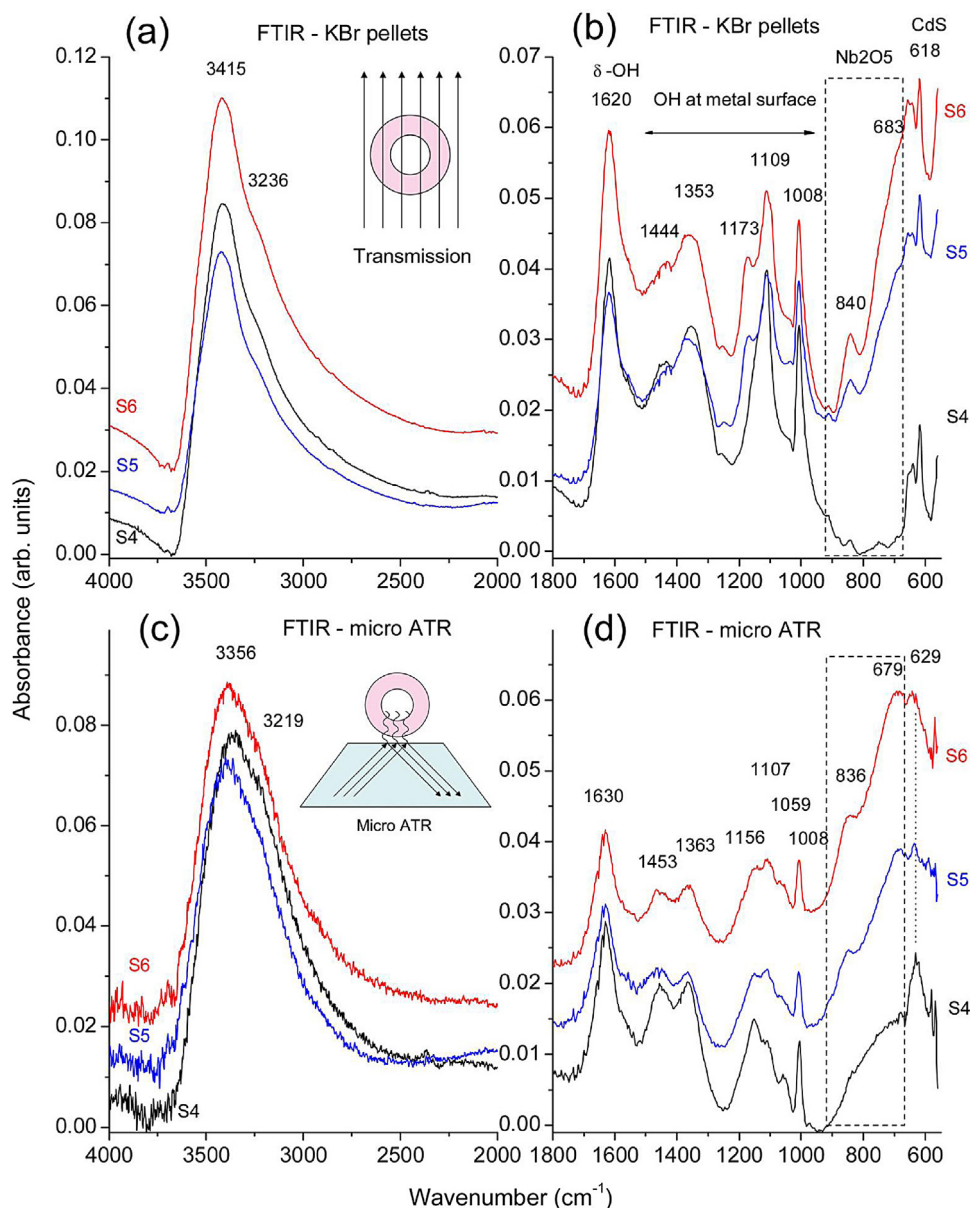


Fig. 2. Raman spectra of samples S4 (a), S5 (b) and S6 (c), for a  $647\text{ nm}$  excitation line, with the characteristic peak positions indicated. The scattering intensities for the spectra above  $560\text{ cm}^{-1}$  have been multiplied by two, in comparison with lower wavenumbers.

The presence of niobium oxide in samples S5 and S6 is revealed by a new (broad) peak that appears at approximately  $985\text{ cm}^{-1}$  for these samples (absent in the S4 Raman spectrum). This peak is characteristic of the Nb=O stretching mode and signifies the presence of crystalline  $\text{Nb}_2\text{O}_5$  in samples S5 and S6 [22]. Additionally, the overall scattering intensity was significantly reduced from S4 to S5 to S6 (the same experimental conditions were used while collecting the spectra). Overall, the independent peak positions for CdS and  $\text{Nb}_2\text{O}_5$  and the decreasing of the intensities of CdS bands were compatible with the proposed core-shell structure: using a  $\text{Nb}_2\text{O}_5$  shell to cover the CdS core diffuses the light and reduces the CdS core's Raman scattering.

The infrared spectra of the samples (S4–S6) between  $4000$  and  $550\text{ cm}^{-1}$  are depicted in Fig. 3. In Fig. 3a, the broad band from  $3700$  to  $3000\text{ cm}^{-1}$  centered at approximately  $3415\text{ cm}^{-1}$  may be assigned to the hydroxyl stretching mode ( $\nu\text{-OH}$ ). This vibrational band was expected because an aqueous synthetic route was used, generating hydroxyl-rich species ( $\text{M-OH}$ ) and hydrogen bonds ( $\text{OH}\cdots\text{OH}$ ). Additionally, co-precipitating the cationic precursors ( $\text{Cd}^{2+}$  and  $\text{Nb}^{5+}$ ) without using a subsequent calcination procedure led to the formation of hydrated groups, such as  $\text{Cd-O-H}$  (S4) or  $\text{Nb-O-H}$  (S5 and S6) that can be identified using characteristic vibrational bands in the region from  $1800$  to  $1000\text{ cm}^{-1}$  (Fig. 3b). Important differences are present in the FTIR spectra between  $1000$  and  $550\text{ cm}^{-1}$  when comparing Sample S4 with Samples S5 and S6. Specifically, the bands at approximately  $840$  and  $680\text{ cm}^{-1}$  may be associated with the vibrational contributions of niobium oxides (crystalline and amorphous, respectively), such as the stretching modes of Nb=O bonds (niobium species) in distorted Nb-O<sub>x</sub> groups and bridging Nb-O-Nb bonds [23–25]. Additionally, a characteristic feature for CdS was observed for all samples as a narrow band at approximately  $618\text{ cm}^{-1}$  [26].

The peak positions and widths for the characteristic bands of niobium oxide and CdS in Fig. 3b remained unchanged between samples S4 to S6, indicating a core-shell ( $\text{CdS-Nb}_x\text{O}_y$ ) nanostructure. To verify this claim, an alternative FTIR technique was used. The spectra in Fig. 3a and b were obtained by transmitting the light through the sample (see the sketch on the inset in Fig. 3a) using



**Fig. 3.** FTIR spectra of samples S4–S6, obtained by transmission through pelletized samples (a and b) or by attenuated total reflection (c and d), in two spectral regions, 4000–2000 cm⁻¹ (a and c) and 1800–550 cm⁻¹ (b and d). The insets in (a) and (c) show the fundamental difference of both techniques: in (a) and (b) the infrared light passes through shell and core (Samples S5 and S6); in (c) and (d) it explores mainly the shell, once the intensity of the evanescent wave decreases exponentially near bands of the shell (the skin depth depends reciprocally on the extinction index).

transparent KBr matrices. In a core–shell structure, the infrared light must pass through both the core and the shell. When comparing the spectra in Fig. 3a and b with those in Fig. 3c and d that were obtained on a micro-ATR using slightly pressed powders (without KBr). In the latter case, the absorbance spectra appeared when the evanescent wave lost energy for the sample. A sketch of this situation is provided in the inset of Fig. 3c. When comparing the higher wavenumber region, Fig. 3a and c reveal that both techniques generate the same features linked to OH stretching modes. The small downshift in Fig. 3c occurred because the techniques were different, and they explored different regions of the samples, as explained below. In the lower wavenumber region, an important difference appeared exactly in the region of interest (below 1000 cm⁻¹): the bands associated with niobium oxide in samples S5 and S6 were enhanced in the micro-ATR spectra (Fig. 3d) relative to the pelletized samples in Fig. 3b. In particular, the broad 680 cm⁻¹ band assigned to amorphous niobium oxide

became very intense. However, the CsS features that appeared at 629 cm⁻¹, which was intense for sample S4, tended to disappear due to the core–shell structure of samples S5 and S6; the high absorption of the Nb<sub>x</sub>O<sub>y</sub> shell centered at 680 cm⁻¹ decreases exponentially as light energy reaches the CdS core (the electric field of the evanescent light decreases as  $\exp(-2\pi\kappa z/\lambda)$ , where  $\kappa$  is the extinction index of the shell, which is very high (approximately 629 cm⁻¹) because the 680 cm⁻¹ band is very broad).

In conclusion, based on the FTIR results, the CdS–Nb<sub>x</sub>O<sub>y</sub> systems were synthesized with a core–shell nanostructure, as evidenced by the niobyl species present in the S5 and S6 sample (not in S4 sample) and the screening effect exhibited on the CdS band when analyzed using reflection techniques (the niobium species encapsulates the CdS particles).

The XRD patterns of the materials are presented in Fig. 4. Every system presented a very similar diffraction pattern that predominantly displayed peaks attributed to the CdS–wurtzite



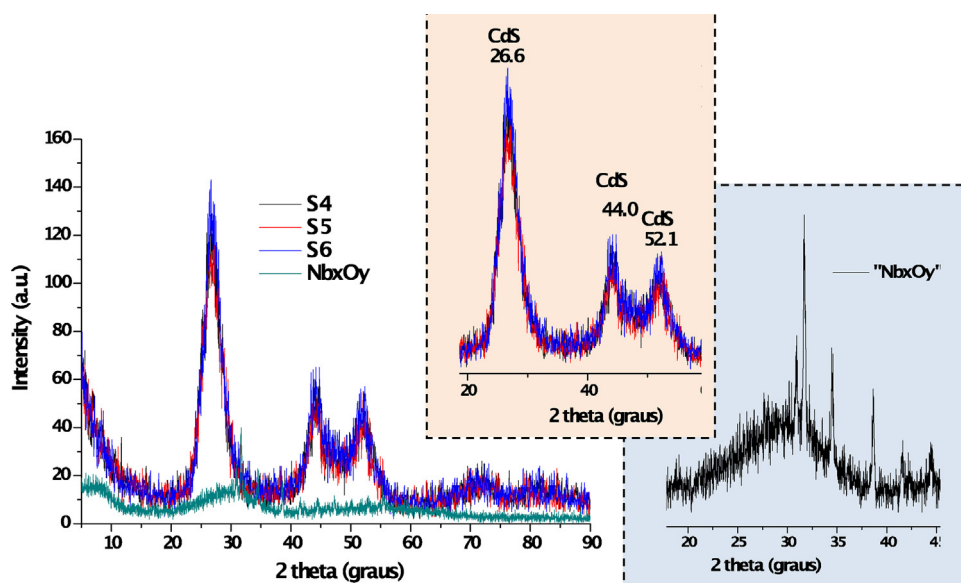


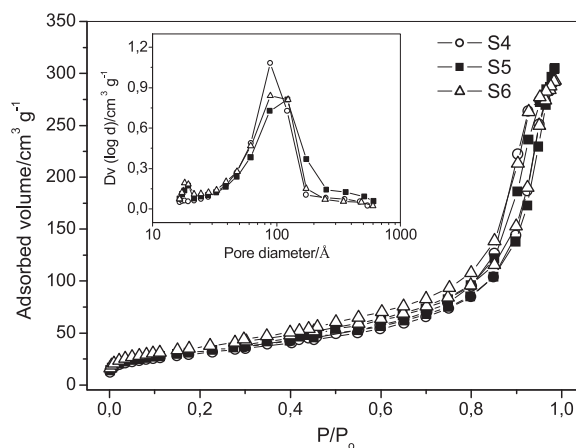
Fig. 4. XRD patterns of S4, S5 and S6 samples.

crystal structure ( $2\theta = 26.6^\circ$ ,  $44.0^\circ$ ,  $52.1^\circ$ , ICDD) regardless of the increasing concentration of  $\text{Nb}_x\text{O}_y$  (0, 5 and 10%) in samples S4, S5, and S6, respectively; these results agreed with the Raman results. These results were expected because the photocatalyst samples containing niobium oxide hydrates (S5 and S6) revealed characteristics of amorphous material (XRD pattern inset Fig. 4) that overlapped with the background signal; this phenomenon is compatible with the aqueous synthesis (no further calcination). Therefore, a nanostructured material was formed with a core-shell ( $\text{CdS}$ , core;  $\text{Nb}_x\text{O}_y$ , shell) morphology and a very small particle size (relative broad diffraction bands), making this material interesting as a catalyst.

The textural characteristics of the materials were determined using  $\text{N}_2$  adsorption/desorption. The isotherms and pore distributions are presented in Fig. 5.

The material synthesized in the presence of niobium (S6 sample) possessed a relative high surface area ( $131 \text{ m}^2 \text{ g}^{-1}$ ) relative to samples without (S4- $109 \text{ m}^2 \text{ g}^{-1}$ ) or less niobium content (S5- $116 \text{ m}^2 \text{ g}^{-1}$ ), revealing that incorporating niobium improves the catalyst's porous structure. More information describing the textural properties of the materials is presented in Table 1. The isotherms in Fig. 5 suggest that the materials are mesoporous. These results were confirmed by the pore distribution (inset) obtained using the B.J.H. (Barrett–Joyner–Halenda) method; pores approximately 100 angstroms in diameter were observed [27].

The UV–Vis absorbance spectra obtained via the diffuse reflectance method are shown in Fig. 6. The conduction band potential ( $E_g$ ) was determined with a Tauc plot using Eq. (1). In Eq. (1),  $A$  is a constant;  $n = 1$  for direct or  $n = 4$  for indirect-band-gap semiconductors;  $\alpha$  is the absorption coefficient;  $fn = 1$  was used in the calculations, and the results are presented in Fig. 6b. There is no consensus yet regarding the direct or indirect transitions of niobium

Fig. 5.  $\text{N}_2$  adsorption/desorption of the S4, S5 and S6 samples.

oxides and their derivative semiconductors [28–30]. That parameter would depend largely on the synthesis: using sol–gel method, with or without calcination, drying and sintering at high temperatures, thermal treatments, crystalline or amorphous phases, and other variables. Nonetheless,  $E_g$  usually falls between 3.0 and 3.4 eV.  $\text{CdS}$  has been broadly accepted as a type II–VI semiconductor with a direct band gap transition suitable for producing fluorescent nanocrystals [31,32]. The  $\text{CdS}$  system (S4) presented  $E_g = 2.43 \text{ eV}$ , as supported by the published value in the literature ( $E_g = 2.4 \text{ eV}$ ). The  $\text{CdS}$ –10% $\text{Nb}_x\text{O}_y$  (S6) system displayed a slightly higher value ( $E_g = 2.5 \text{ eV}$ ) that was compatible if a core-shell nanostructure of  $\text{CdS}$ – $\text{Nb}_x\text{O}_y$  was assumed because a semiconductor with a wider band gap (shell) shifts toward higher energy.  $\text{Nb}_2\text{O}_5$

**Table 1**  
Band Gap of the S4–S6 samples.

Sample	"Band gap" $\lambda$ (nm)	"Band gap" energy by Tangent of reflectance (curves) (eV)	"Band gap" energy by optical "Tauc" <sup>a</sup> (eV)	
			Graphic	Derivative
$\text{Nb}_2\text{O}_5$ reference	319.8	3.90	3.70	3.40
S4	500.5	2.48	2.43	2.27
S5	492.0	2.52	–	–
S6	497.5	2.49	2.47	2.32

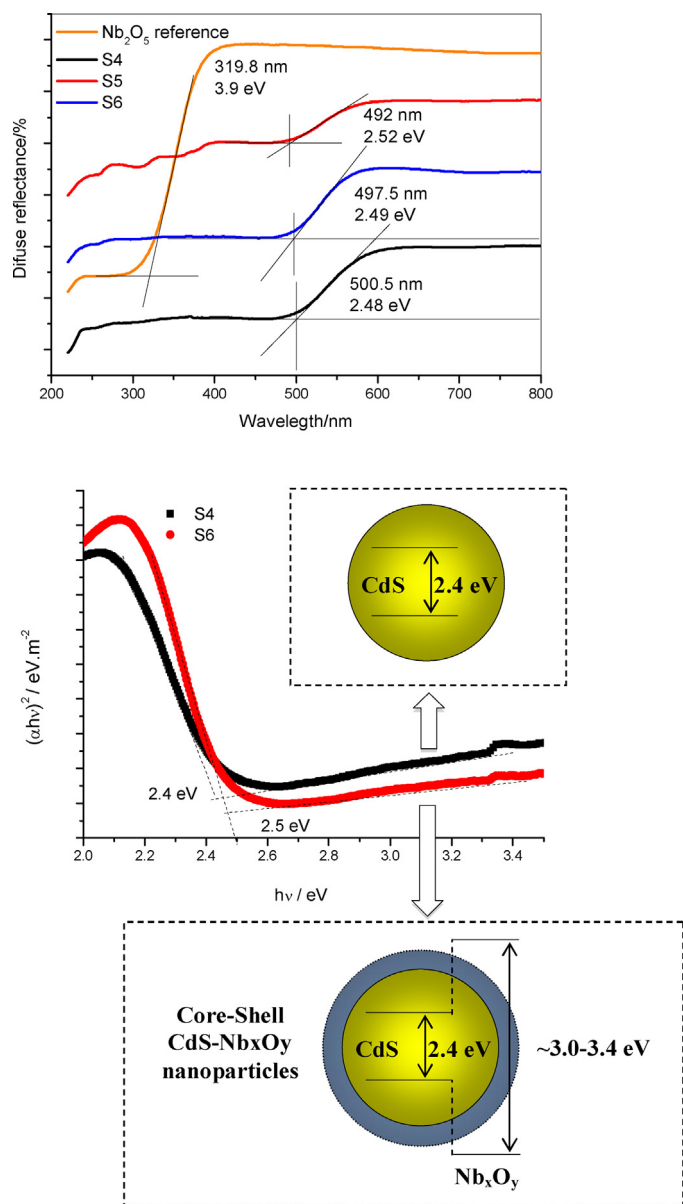


Fig. 6. UV-Vis absorbance spectra obtained by diffuse reflectance method.

is an n-type semiconductor with a wide-band-gap and a conduction band comprised of empty  $\text{Nb}^{5+}$  4d orbitals. Consequently, combining a CdS-core with a  $\text{Nb}_x\text{O}_y$  shell would account for the intermediate value measured for the band gap of ( $E_g = 2.5$  eV) the S6 sample that fell between 2.4 eV (CdS) and 3.0 eV (Nb oxides).

These results suggested that generating an electron-hole pair and hydroxyl radicals should be facilitated by these materials, giving them potential as photocatalysts capable of using solar radiation and decreasing process costs. The band gap was calculated using Eq. (1):

$$\alpha h\nu = A(h\nu - E_g)^{n/2} \quad (1)$$

where  $\alpha$ ,  $E_g$ ,  $\nu$  and  $A$  are the absorption coefficient, band gap, light frequency, and  $A$  constant, respectively [21]. The calculated band gap is revealed in Table 1.

The results of PL are presented in Fig. 7. The relative photoluminescent response decreased as the niobium concentration increased; this effect is consistent with a core-shell nanostructure. Therefore, the CdS nanocrystals (S4) exhibit the maximum

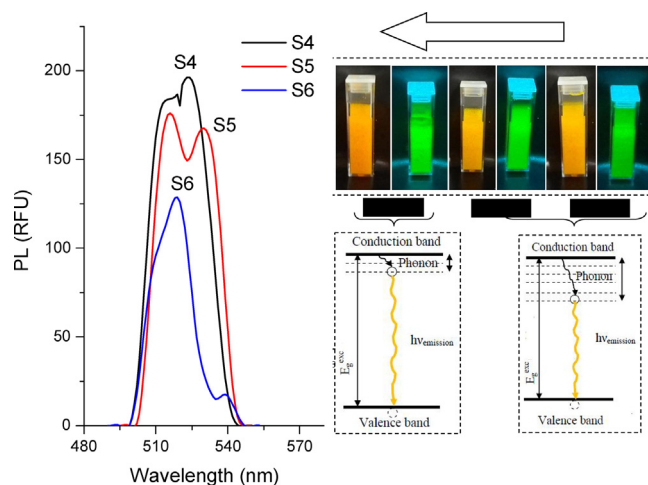


Fig. 7. Photoluminescent of the S4, S5 and S6 samples.

PL response after excitation in the visible range of the electromagnetic spectrum (white light). However, forming a shell with a wider band gap semiconductor ( $\text{Nb}_x\text{O}_y$ ) would require a higher excitation energy to generate the electron-hole excited state and facilitate the later recombination via PL emission (radiative decay). Additionally, forming amorphous niobium oxide hydrates shells (S5 and S6) may have caused structural lattice mismatches (CdS core) that may behave as trap states. Therefore, the concentrated trap states on the semiconductor nanocrystals are dominant channels for the nonradiative decay of carried charge [33], as depicted in Fig. 7 (inset).

The particles' morphology, shape, and size distribution were examined with a JEOL JEM 2100 transmission electron microscope. The samples used for transmission electron microscopy (TEM) analysis were prepared by drying a hexane dispersion of the particles on amorphous carbon-coated copper grids.

The effect of the addition of  $\text{Nb}^{5+}$  cations during the synthesis of the catalysts on their morphology was evaluated through TEM images shown in Fig. 8 (left column). TEM images showed that the morphology is similar for the material with and without niobium, presenting agglomerates of spherical particles. The electron diffraction (ED) pattern of the bare nanoparticles (S4) and core portion (S5 and S6) showed a lattice parameter comparable to the CdS wurtzite crystalline structure (sketch drawing, inset of Fig. 8a, right column). The chemical analysis by EDS spectroscopy indicated Cd and S as the major elements, excluding the copper and carbon peaks from the TEM grid and Si from the detector. Core-shell structures also presented niobium in the material (Fig. 8b right column). High resolution TEM micrographs of CdS- $\text{Nb}_x\text{O}_y$  core-shell nanostructures are shown in Fig. 8c right column. The spherical core and covering shell can be observed. Under TEM conditions, the highest atomic number of CdS makes the darkest images. Additionally, niobium oxide hydrates prepared by aqueous precipitation method are usually amorphous, which may be detected by the lack of diffraction pattern in the SAED (selected area electron diffraction) analysis.

Fig. 9 reveals the wide size distribution (4–15 nm) of the materials. In addition, a small decrease in the particle size was observed after niobium was incorporated in the S5 and S6 catalysts.

### 3.2. Catalytic tests

The dye discoloration studies were carried out using a cationic organic dye: methylene blue. This dye is suitable for probing molecular oxidation reactions: (i) they are highly soluble in water,

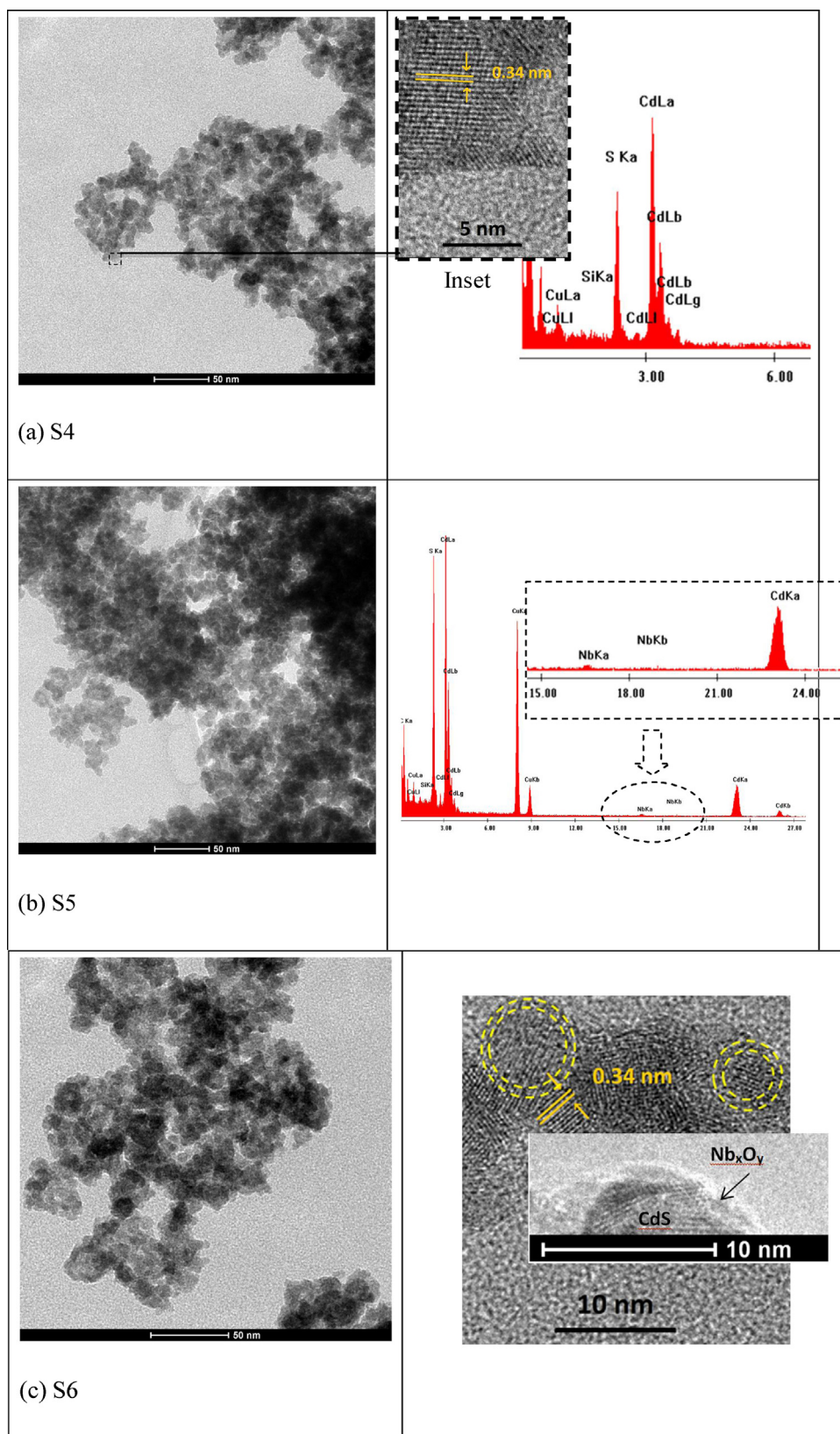


Fig. 8. TEM/EDS analyses of the S4 (a), S5 (b) and S6 (c) samples.

(ii) their discoloration reactions can be monitored with simple spectrophotometric measurements and (iii) they simulate the behavior of textile dyes, which are an important class of contaminants [3].

The materials were tested as catalysts in the presence of both visible and UV radiation. The results are presented in Fig. 10a. The discoloration profile at 663 nm for the solution containing methylene blue dye reveals that the niobium-modified cadmium

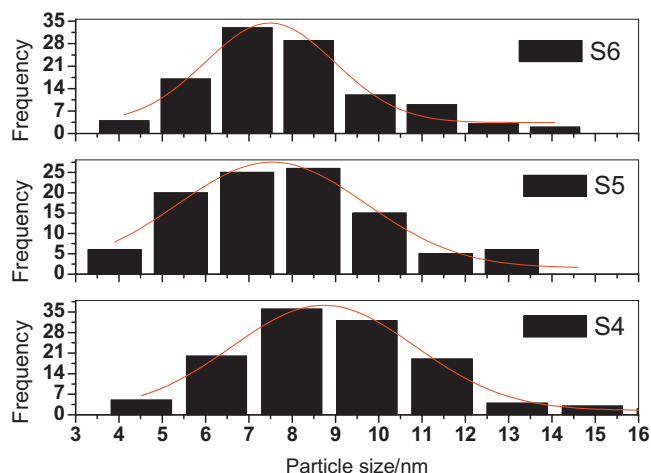


Fig. 9. Particle size distribution obtained from a set of TEM images.

sulfide removes the dye from the aqueous medium competently. The material modified with 10% of niobium (S6) removed approximately 70% of the coloration after a 30 min reaction under visible light. The cadmium sulfide without niobium (S4) removed approximately 30% under the same conditions. Much like data for the diffuse reflectance of solids, the niobium promotes a shift in the absorption toward lower energies, facilitating the formation of an electron-hole pair and consequently the  $^{\bullet}\text{OH}$ . The color removal tests were conducted in the dark to verify that the discoloration had

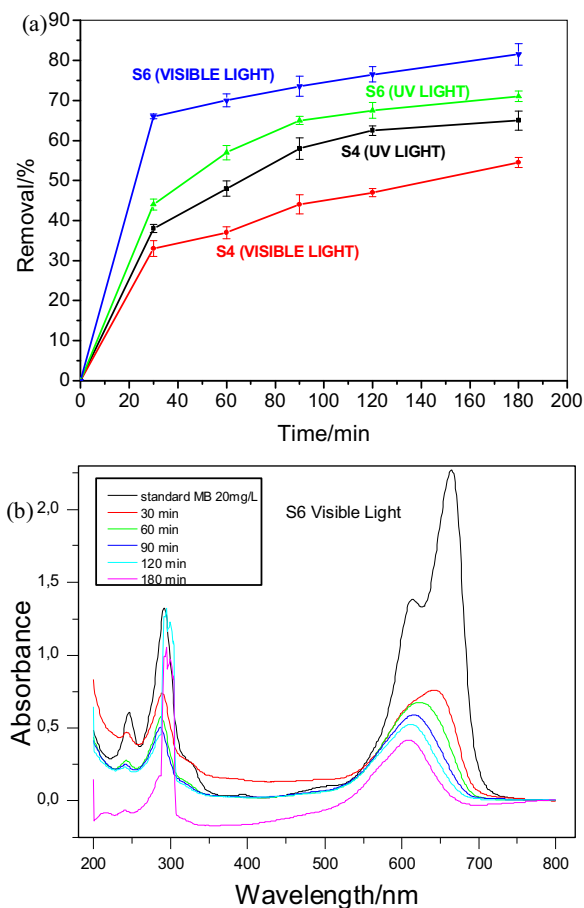


Fig. 10. Profile (a) and scan (b) of methylene blue color removal by photocatalysis reactions in the presence of S4 and S6 samples under visible and UV light.

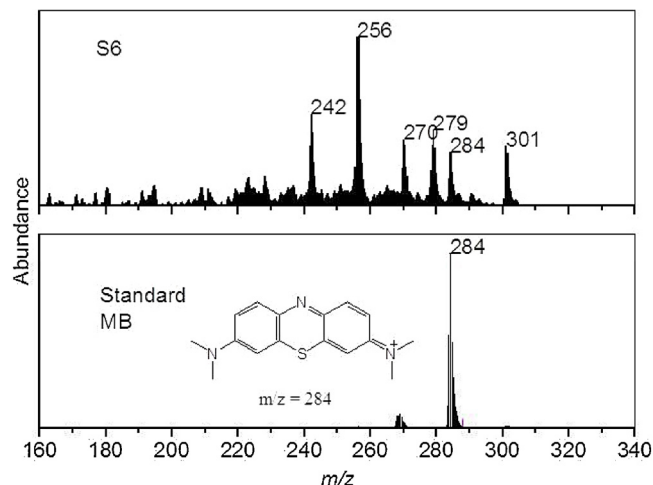


Fig. 11. ESI-(+)-MS of methylene blue dye after 180 min of reaction in the presence of S6 sample (a) and standard solution (b).

not occurred through adsorption (not shown here). The materials removed much less dye when only utilizing adsorption processes. Fig. 10b reveals the scan spectra for the organic dye solution signal describing the dye removal during the reaction using the S6 catalyst. Furthermore, the maximum adsorption displacement suggests new compounds were formed, suggesting that the organic pollutants were degraded. The UV–Vis spectra for other catalysts follow the same trend and presented as supplementary material (Figure S1).

The degradation of the dye molecule was confirmed using the ESI–MS path, as described in Fig. 11. The ESI–MS experiments using methylene blue (MB) and the S6 catalyst (Fig. 11a) revealed a strong signal at  $m/z = 301$  most likely arising from the successive hydroxylation of the MB aromatic ring. These data strongly suggest that the reaction using this catalyst is initiated by the  $^{\bullet}\text{OH}$  radicals produced during the photocatalytic process [12]. Moreover, at reaction time zero, the ESI–MS, when operating in positive mode, revealed only a single cation ( $m/z = 284$ ) in the aqueous solution (Fig. 12b). After a 60 min reaction, the intense peak at  $m/z = 284$  diminished, and new peaks with  $m/z = 279, 270, 256$  and  $242$  emerged (Fig. 11a).

Organic compounds may be hydroxylated by the reactive  $^{\bullet}\text{OH}$  radical, leading to successive oxidation/addition and eventual ring opening, as depicted in Fig. 11. During heterogeneous

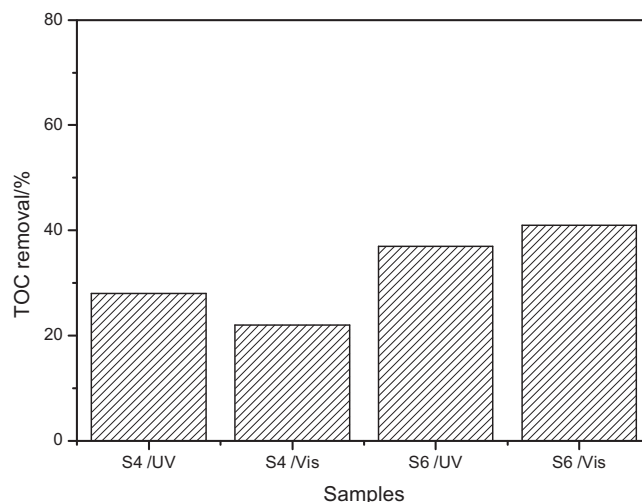


Fig. 12. Total organic carbon analyses for the S4 and S6 samples.



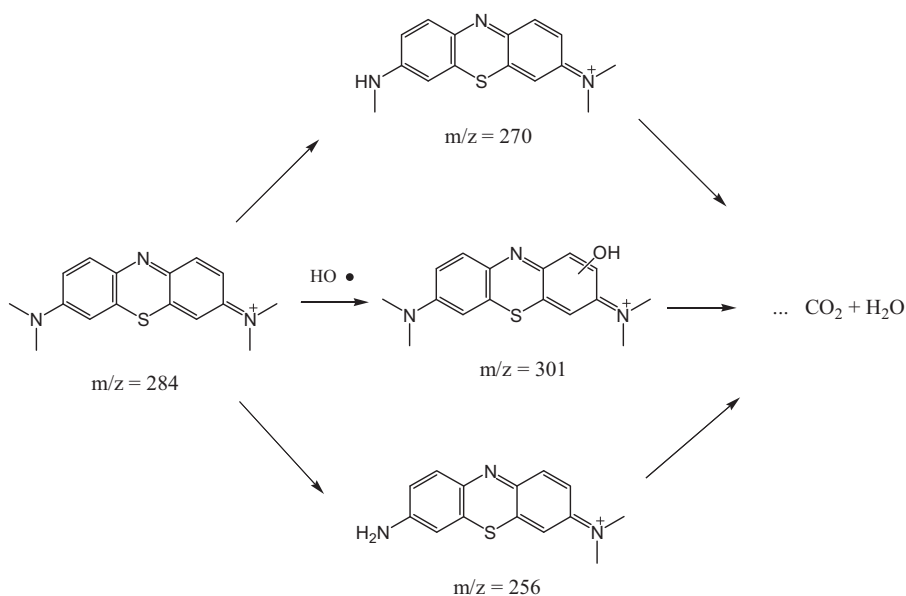
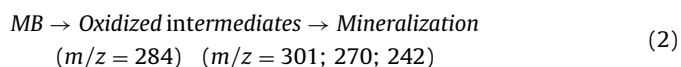


Fig. 13. Proposed intermediate species from methylene blue dye oxidation.

photocatalysis, the liquid phase organic compounds are degraded to their corresponding intermediates and further mineralized to form carbon dioxide and water after extended irradiation times (Eq. (2)). Fig. 12 shows the TOC removal for the sample S4 and also S6 after 180 min of reaction. It can be observed that the Nb presence (S6 sample) produced a higher TOC removal (approximately 41% removal in 180 min of contact time) than the material without Nb (S4 sample), suggesting that the presence of niobium phases might play a role in the removal process. It is interesting to note that the removal of TOC indicates the reaction intermediates observed via ESI structures are likely to be completely oxidized contributing to the removal of the organic load of the solution. The main intermediates species are displayed in Fig. 13.



The photocatalyst improved dye oxidation in the presence of Nb species due to the core-shell structure; this structure increased the donor concentration and therefore improved the conductivity and charge transfer while decreasing carrier recombination. Moreover, the energy level for the conduction band edge in  $\text{Nb}_x\text{O}_y$  can inject electrons into the conduction band of CdS, improving the  $^*\text{OH}$  generation and further hydroxylating the organic dye (Fig. 11). Additionally, forming an amorphous niobium oxide hydrate shell may have caused a structural lattice mismatch (CdS core), generating trap states that decreased the electron-hole recombination and improved the oxidation reaction. Control experiments using only radiation and pure niobium oxide were performed presenting negligible capacity for photodegradation of the dye.

#### 4. Conclusions

The synthesis of a nanostructured niobium-modified cadmium sulfide exhibited increased photocatalytic activity, as evidenced by the increased color removal and the formation of reaction intermediates observed by ESI-MS. The presence of niobium improved the photocatalytic properties of the materials by decreasing the band gap, facilitating the increased generation of strong oxidants (hydroxyl radicals). The untreated material displayed a significant removal percentage through adsorption processes without exhibiting a significant photocatalytic effect. Photocatalysis using sunlight

may be an efficient and promising process due to the use of natural light; these processes would not demand the use of special facilities for generation of ultraviolet radiation, making them less onerous.

#### Acknowledgments

The financial support from the CNPq, CAPES and FAPEMIG is gratefully acknowledged. The authors thank the Staff of Microscopy Center/UFGM for the TEM/EDS analyses.

#### Appendix A. Supplementary data

Supplementary material related to this article can be found, in the online version, at <http://dx.doi.org/10.1016/j.apcatb.2014.01.025>.

#### References

- [1] M. Ziolk, P. Decyk, I. Sobczak, M. Trejda, J. Florek, H. Golinska, W. Klimas, A. Wojtaszek, *Appl. Catal.*, A 391 (2011) 194–204.
- [2] D.Q.L. Oliveira, M. Goncalves, L.C.A. Oliveira, L.R.G. Guilherme, J. Hazard. Mater. 151 (2008) 280–284.
- [3] S.B.C. Pergher, L.C.A. Oliveira, A. Smaniotto, D.I. Petkowicz, *Quim. Nova* 28 (2005) 751–755.
- [4] A. Florentino, P. Cartraud, P. Magnou, M. Guisnet, *Appl. Catal.*, A 89 (1992) 143–153.
- [5] L.C.A. Oliveira, F. Zaera, I. Lee, D.Q. Lima, T.C. Ramalho, A.C. Silva, E.M.B. Fonseca, *Appl. Catal.*, A 368 (2009) 17–21.
- [6] M.A. Abdel-Rehim, A.C.B. Santos, V.L.L. Camorim, A.C. Faro, *Appl. Catal.*, A 305 (2006) 211–218.
- [7] R.C. Pawar, Caroline Sunyong Lee, *Mater. Chem. Phys.* 141 (2013) 686–693.
- [8] R.C. Pawar, Caroline Sunyong Lee, *Appl. Catal.*, B 144 (2014) 57–65.
- [9] A. Kunz, P. Peralta-Zamora, S.G. Moraes, N. Duran, *Quim. Nova* 25 (2002) 78–82.
- [10] C.R.L. Souza, P. Peralta-Zamora, *Quim. Nova* 28 (2005) 226–228.
- [11] A. Kudo, Y. Miseki, *Chem. Soc. Rev.* 38 (2009) 253–278.
- [12] L.C.A. Oliveira, T.C. Ramalho, E.F. Souza, M. Goncalves, D.Q.L. Oliveira, M.C. Pereira, J.D. Fabris, *Appl. Catal.*, B 83 (2008) 169–176.
- [13] C.S. Castro, M.C. Guerreiro, L.C.A. Oliveira, M. Goncalves, A.S. Anastacio, M. Nazzarro, *Appl. Catal.*, A 367 (2009) 53–58.
- [14] Ramanathan Sundararaman, Chunshan Song, *Appl. Catal.*, B 148–149 (2014) 80–90.
- [15] Jan Ungelenk, Claus Feldmann, *Appl. Catal.*, B 102 (2011) 515–520.
- [16] Zhichao Liu, Zhifeng Liu, Ting Cui, Junwei Li, Jing Zhang, Tao Chen, Xingchen Wang, Xiaoping Liang, Photocatalysis of two-dimensional honeycomb-like ZnO nanowalls on zeolite, *Chem. Eng. J.* 235 (2014) 257–263.
- [17] C. Li, T. Ahmeda, M. Mab, T. Edvinsson, J. Zhu, *Appl. Catal.*, B 138–139 (2013) 175–183.

- [18] U. Venkateswaran, M. Chandrasekhar, H.R. Chandrasekhar, *Phys. Rev. B: Condens. Matter* 30 (1984) 3316–3319.
- [19] H. Poulet, J.P. Mathieu, *Ann. Phys.* 9 (1964) 549.
- [20] M. Balkanski, J.M. Besson, R. Toullec, *Proc. 7th Int. Conf. Phys. Semicond. Paris* (1964) p1091.
- [21] M.A. Nusimovici, M. Balkanski, J.L. Birman, *Phys. Rev. B: Condens. Matter* 1 (1970) 595–603.
- [22] B.X. Huang, K. Wang, J.S. Church, Y.S. Li, *Electrochim. Acta* 44 (1999) 2571–2577.
- [23] W.F. Souza, I.R. Guimaraes, M.C. Guerreiro, L.C.A. Oliveira, *Appl. Catal., A* 360 (2009) 205–209.
- [24] D. Prasetyoko, Z. Ramli, S. Endud, H. Nur, *Adv. Mater. Sci. Eng.* 2008 (2008) 1–12.
- [25] V.S. Braga, J.A. Dias, S.C.L. Dias, J.L. Macedo, *Chem. Mater.* 17 (2005) 690–695.
- [26] M. Paulis, M. Martín, D.B. Soria, A. Díaz, J.A. Odriozola, M. Montes, *Appl. Catal., A* 180 (1999) 411–420.
- [27] S.J. Gregg, K.S.W. Sing, *Adsorption Surface Area and Porosity*, Academic Press, New York, NY, 1982.
- [28] F. Lenzmann, V. Shklover, K. Brooks, M.J. Grätzel, *Sol–Gel Sci. Technol.* 19 (2000) 175–180.
- [29] H. Luo, W. Song, P.G. Hoertz, K. Hanson, R. Ghosh, S. Rangan, M.K. Brennaman, J.J. Concepcion, R.A. Binstead, R.A. Bartynski, R. Lopez, T.A. Meyer, *J. Chem. Mater.* 25 (2013) 122–131.
- [30] K. Nakajima, Y. Baba, R. Noma, M. Kitano, J.N. Kondo, S. Hayashi, M. Hara, *J. Am. Chem. Soc.* 133 (2011) 4224–4227.
- [31] H.S. Mansur, J.C. González, A.A.P. Mansur, *Colloids Surf., B* 84 (2011) 360–368.
- [32] H.S. Mansur, J.C. González, A.A. Mansur, *Polymer* 52 (2011) 1045–1054.
- [33] A.A.P. Mansur, F.P. Ramanery, H.S. Mansur, *J. Mater. Chem.* 1 (2013) 1696–1711.